Subpixel Variability and Quality Assessment of Satellite Sea Surface Temperature Data Using a Novel High Resolution Multistage Spectral Interpolation (HRMSI) Technique

Sandra L. Castro[1,*], Lucas A. Monzon[2], Gary A. Wick[3], Ryan D. Lewis[2,†], and Greg Beylkin[2]

[1]Colorado Center for Astrodynamics Research, University of Colorado, Boulder, CO, USA.

[2]The Numericus Group, LLC, Boulder, CO, USA.

[3]NOAA Earth System Research Laboratory, Physical Sciences Division, Boulder, CO, USA.

Revised for *Remote Sensing of Environment*

August 13, 2018

*Corresponding author address: Colorado Center for Astrodynamics Research, University of Colorado, 431 UCB, Boulder, CO 80309, USA; E-mail address: sandrac@colorado.edu

[†]Currently with Google Inc., Boulder, CO.

Abstract

A novel interpolation technique is applied to assessment of the quality of sea surface temperature (SST) observations and quantitative analysis of the subpixel variability within satellite footprints of different size. Using retrieved satellite data as input, the new, global, multistage interpolation technique generates a trigonometric polynomial, providing a representation of the underlying physical SST field in functional form. The resulting interpolating function can be efficiently and accurately evaluated anywhere within the domain over which it was derived and its moments calculated to estimate the mean and variance of the field over desired sub-regions. Application of the technique is demonstrated for SST retrievals from the Moderate Resolution Imaging Spectroradiometer (MODIS), Spinning Enhanced Visible and Infrared Imager (SEVIRI), and Advanced Microwave Scanning Radiometer - Earth Observing System (AMSR-E) sensors. Comparison of the functional form with the data from which it was derived demonstrates how the technique can potentially help to identify small observational artifacts such as MODIS scan striping and residual cloud contamination. Integrals of the interpolating functions over successively larger spatial scales successfully emulate the retrieved SST at the different effective spatial resolutions and the second moments are consistent with the direct sample variances, and hence representative of the spatial SST variability of the available finer-resolution observations over the coarser scales. Using the approach, the variability of 1-km-resolution SST observations on open ocean grids of both 5- and 25-km resolution is found to be ~0.07 K. In regions of sharper gradients such as associated with strong localized diurnal warming, the variability within 25-km-resolution grids increases to as much as 0.4 K for sampling at 1-km resolution. The variability of 1-km observations on a 25-km-resolution grid is about 2.4 times greater than that on a 5-km-resolution grid. Broader application of the technique globally could help better

47 quantify regional variations in the spatial variability, which would subsequently improve
48 uncertainty estimates for existing satellite-based SST products.
49
50
51 Keywords: SST subpixel variability; spatial variability; interpolation techniques
52

1. Introduction

Interpolation methodologies are widely employed in the analysis and application of sea surface temperature (SST) products and imagery. The most common usage is to fill gaps in the spatial coverage of the available products. The capabilities of certain new approaches, however, enable promising additional unique and valuable applications. In this paper, we show that a novel High Resolution Multistage Spectral Interpolation technique (HRMSI) can be applied to assessment of the quality of the underlying SST observations and analysis of the subpixel variability within satellite footprints of different size.

Multiple techniques have been developed and utilized to fill gaps in satellite SST imagery, particularly for providing spatially complete, daily SST analyses (level 4 products, e.g. Martin et al., 2012). Gaps in the spatial coverage of the retrieved satellite products result from many interfering factors such as clouds, precipitation, and aerosols. Atmospheric constituents can confound the radiative signal from the earth's surface, either degrading the accuracy of the physical retrievals or obscuring them completely. The source and size of the gaps is specific to the retrieved variable and the portion of the electromagnetic spectrum being utilized. For infrared retrievals of SST, clouds are the primary challenge, completely attenuating the infrared radiation emitted by the surface. Within the microwave portion of the spectrum, the radiation can pass through non-precipitating clouds, but regions of precipitation still obscure the surface. Gaps also clearly result from limited sensor swaths, particularly in the equatorial regions for polar-orbiting satellites.

Interpolation methods utilized in the generation of spatially complete SST products have been based largely on variations of the so-called optimal interpolation technique (e.g. Reynolds and Smith, 1994; Reynolds et al. 2007). The review by Martin et al. (2012) provides a good

76 overview of many current SST analyses and the different approaches used in their generation.
77 An additional approach for the reconstruction of missing data using empirical orthogonal
78 function (EOF) decomposition applied to several oceanographic variables was described by
79 Alvera-Azcárate et al. (2007) and a more recent technique for multiscale interpolation involving
80 the use of wavelets has been applied to SST fields by Chin et al. (2017). While largely
81 consistent and extensively utilized, the quality of the analyzed products remains variable,
82 particularly for regions of high spatial variability such as current systems, temperature fronts,
83 and coastal and polar oceans (Reynolds and Chelton, 2010; Martin et al., 2012; Dash et al., 2012;
84 and Castro et al., 2016), and further improvement in the quality of the products is desirable.
85 Many other interpolation/regression techniques address practical problems associated
86 with fitting scattered and noisy data with potentially large gaps. One comparison of several
87 different techniques applied to the gridding of multiple climate variables was presented by
88 Hofstra et al. (2008). The techniques differ in complexity and their utilization of the available
89 frequency content of the data, which, in turn, is determined by the sampling density.
90 Of particular interest here is the ability of an interpolation technique to provide an
91 explicit functional representation of the data as opposed to discrete interpolated values at
92 selected points of interest. Such a functional form enables not only the evaluation of the
93 interpolant at any arbitrary point within the domain of interest, but also the computation of a
94 variety of quantities such as derivatives and integrals in analytic form. While fully applicable to
95 the traditional problem of gap filling in satellite imagery and construction of level 4 SST
96 products, the functional form and the above-mentioned properties offer the potential to address
97 other significant problems impacting the assessment of SST retrieval quality and better
98 quantification of the full uncertainty budget for the SST products.

One such data quality issue is identification of instrumental or processing "artifacts" within the retrieved satellite data related to the way in which the sensors operate or the product is constructed. While highly useful, satellite products are known to have important issues that can be extremely difficult to identify. Scan striping is a particularly important example. Sensors employing arrays of detectors like the Moderate Resolution Imaging Spectroradiometer (MODIS, Esaias et al., 1998) and the Visible Infrared Imaging Radiometer Suite (VIIRS, Murphy et al., 2006) are subject to issues with consistency in the calibration of the individual array detectors that can lead to the appearance of "stripes" or distortions in the derived products along instrument scans (Bouali and Ignatov, 2014). Accurate identification and removal of these artifacts is complicated, and despite significant efforts by the data providers, current products in use can still exhibit some features of the artifacts.

Another prominent problem is accurate determination of the spatial SST variability within the footprints of different resolution products and its impact on validation and merging of the retrievals. Validation of satellite SST products relies primarily in situ measurements from drifting and moored buoys as well as radiometric measurements collected from research vessels and ships-of-opportunity. These in situ sensors provide "point" measurements, which are then compared with larger areal averages from the satellite-borne radiometers. This mismatch in spatial resolution directly affects the perceived accuracy of the satellite retrievals when validated in this manner. The contribution of subpixel variability to the overall uncertainty budget of satellite SST retrievals has long been acknowledged (e.g., Minnett, 1991; Cornillon et al., 2010; Castro et al., 2017), but has yet to be fully quantified due to measurement limitations. Accurate estimation of the spatial variability is dependent on complete, high-resolution sampling of the region of interest. Satellite data, however, is often incomplete due to the gaps described above

122 and is limited by the sensor resolution. Techniques such as variogram analysis (Castro et al.,
123 2010; Kent et al., 1999, Cressie 1993) enable estimates of variability on larger scales to be
124 downscaled but the results are still highly dependent on the quality and density of the available
125 observations. The availability of an accurate fit to the data in functional form would provide a
126 new way of estimating the fundamental SST variability since the function could also be
127 integrated over arbitrary satellite footprints. Moreover, since the variance, σ^2, of the SST
128 distribution within a satellite's footprint is a measure of the subpixel variability, the second
129 moment of the interpolating function could be explicitly evaluated to yield the predicted value of
130 σ^2 at different spatial scales.

131 In this paper, we address these problems through application of a novel global
132 interpolation/regression methodology employing trigonometric polynomials (i.e. sinusoidal
133 functions, hence the name trigonometric interpolation) that yields an explicit functional
134 representation of the retrieved satellite data. While the utility of intelligently filling coverage
135 gaps with a physically realistic and continuous functional form is clear, this paper does not focus
136 on this aspect or a comparison of this methodology with other techniques. Rather, the primary
137 emphasis here is on retrieval quality assessment and spatial variability of satellite SSTs.
138 Following a brief description of the technique (Section 2) and the satellite data sets employed
139 (Section 3), the basic capabilities and limitations of the technique are shown in Section 4.
140 Broader application of the technique is illustrated in Section 5 along with a demonstration of
141 how it can help identify problems associated with scan striping, instrument artifacts, and residual
142 cloud contamination, and be employed as a tool for objective quality data assessment and
143 flagging. In Section 6, the moments of the interpolants for the different satellite SST sensors and

144 grid resolutions are evaluated and employed to explicitly quantify the spatial variability across
145 broad regions and different spatial scales.
146
147 **2. New Trigonometric Interpolation Methodology**
148 The new global interpolation methodology applied in this paper employs trigonometric
149 polynomials obtained using a multistage approach. It is well understood that global
150 interpolation/regression approaches are able to capture a significantly greater frequency range
151 (and thus achieve higher resolution) than local techniques. For a simple example, assuming
152 periodicity and uniform sampling, trigonometric polynomial interpolation requires only two
153 points per wavelength, whereas any standard polynomial-based or local interpolation techniques
154 would require a significant oversampling factor to attain the same spatial resolution. The
155 problem with attempting a direct global interpolation on scattered data, however, is that
156 variations in data density will force a lower global resolution, losing the advantage over local
157 interpolation. By introducing a multistage approach, we can accommodate regions of very
158 different data density without resorting to the oversampling factor present in purely local
159 interpolation techniques. Starting from a coarse scale, we gradually increase the interpolant
160 resolution in stages as we partially fill the gaps in the data. The resulting image has adequate
161 resolution in the gaps and the best possible high resolution in the regions with sufficient data
162 density. In so doing, high frequencies present in the input data associated with noise or other
163 nonphysical effects can also be removed. The method shares many similarities with the
164 approach of Chin et al. (2017) but the main difference is that our technique is global rather than
165 local in nature. This section provides a brief mathematical introduction to the technique. While

its application to SST fields is the subject of this paper, the technique can be applied to scattered measurements of physical fields of any type.

A standard trigonometric interpolation assumes a functional form of the target image in terms of a real-valued trigonometric polynomial (that is, a finite (truncated) Fourier series),

$$I(x,y) = \sum_{|k|\le K,|l|\le L} c_{kl} e^{2\pi ikax + 2\pi ilby}, \quad (1)$$

for some coefficients c_{kl}, positive integers K and L, and positive (scaling) constants a and b. Note that we can also write (1) as

$$I(x,y) = \sum_{0\le k\le K,0\le l\le L} a_{kl}\cos(2\pi kax + 2\pi lby) + b_{kl}\sin(2\pi kax + 2\pi lby),$$

using real-valued coefficients a_{kl} and b_{kl}. To simplify the description, we assume that $K = L = L_{final}$ and say that L_{final} is the *degree* of the trigonometric polynomial $I(x,y)$. Thus, L_{final} determines the highest resolution that can be achieved by this trigonometric polynomial representation. If the input data were available on a (sufficiently dense) uniform grid, then the coefficients c_{kl} could be easily estimated using the Fast Fourier Transform (FFT). The satellite retrieved values $\{t_n\}_n$, however, are available at irregular (scattered) points $\{(x_n, y_n)\}_n$ corresponding to coordinates of longitude, x_n, and latitude, y_n. For this reason, to determine the coefficients c_{kl}, we have to solve a least squares problem of the form $\sum_{|k,l|\le L_{final}} c_{kl} e^{2\pi ikax_n + 2\pi ilby_n} = t_n$. Unfortunately, for a typical irregular grid, this formulation leads to an ill conditioned problem. As a result, we would be forced to use a lower order trigonometric polynomial (i.e., to accept a low degree L_{final}). Our multistage approach to build the function I avoids this problem as follows.

Our first step is to approximate the data using a low degree L_0, i.e., we solve the weighted linear squares problem (with weights based on the local grid density)

$$\sum_{|k,l|\le L_0} c^0_{kl} e^{2\pi ikax_n + 2\pi ilby_n} = t_n, \quad (2)$$

to find coefficients c_{kl}^0 for a small L_0. With these coefficients, we build the trigonometric polynomial

$$I_0(x,y) = \sum_{|k,l|\leq L_0} c_{kl}^0 e^{2\pi ikax + 2\pi ilby}.$$

This step, by itself, can also be interpreted as denoising the data since high frequency noise is suppressed in the representation. Once I_0 is estimated, we use it to partially fill existing gaps in the data, which allows us to generate an augmented data set consisting of the initial set and the newly filled locations and their corresponding estimated temperatures. At the next stage, we use the newly built, larger input data set to solve a system of the form (2), but where we can now increase the value of the degree of the trigonometric polynomial from L_0 to (a larger) L_1without causing ill-conditioning. The improved condition number (a factor controlling the sensitivity of the solution to small variations in the input data) for the larger system is due to the information added/gained through data augmentation. Solving this augmented system, we find coefficients c_{kl}^1, which we use to build a new estimate I_1. This I_1 is used to further reduce the gaps in the data and build a new system of the form (2), now with $L_2 > L_1$. We continue in this manner until we reach the final degree, L_{final} , yielding our final interpolant $I(x,y)$. Although this final degree should never exceed the degree implied by the region of highest density of measurements, it is also chosen to avoid overfitting by accounting for the level of measurement noise.

As a step in solving the least squares problem, we evaluate trigonometric sums on unequally spaced grids. For this purpose, we use the Unequally-Spaced Fast Fourier Transform (USFFT) (Dutt and Rokhlin, 1993; Beylkin, 1995) to assure both speed and accuracy.

In order to efficiently and accurately evaluate the resulting interpolating function (the trigonometric polynomial in (1)), on any uniform or non-uniform grid, we once again use the USFFT. The USFFT has the same complexity as the FFT and its actual cost is only a small

212 factor greater than that of FFT. Note that for strictly uniform grids, the FFT may be more
213 efficient, but for cases where the input requires significant padding, the USFFT is also a better
214 choice. Unlike other more common interpolation techniques, our method can be understood as a
215 regression technique since the values of the interpolating function at the original sample
216 locations may not coincide with the values of the input data. In other words, evaluation of the
217 interpolant $I(x, y)$ at the original observation points yields predicted values, not the original
218 retrievals. In this manner, analysis of the residuals (interpolation error) can help identify
219 potential measurement errors and processing artifacts in the satellite retrievals.
220 Furthermore, the interpolating function can be accurately integrated over any domain. In
221 particular, it permits the explicit computation of the statistical moments of the SST distribution.
222 Of relevance for the application considered in this paper is the evaluation of the second moment
223 (variance) as it yields a measure of the SST variability at selected points and spatial scales.
224 If several interpolating functions are available for overlapping regions, it is easy to
225 combine them in a consistent way since they can be evaluated on a sufficiently dense common
226 grid. In fact, any other convenient functional representation could be used for the result of such
227 combination. Thus, global SST maps can be obtained for all ocean basins and then combined
228 with a minimal additional computational cost. One of the remaining problems is to estimate the
229 temperature near continental boundaries. With our technique small islands can be treated as gaps
230 and, after filling the gaps, the resulting interpolation can be restricted to open ocean areas. In the
231 case of a large land mass, additional techniques need to be developed to take into account
232 relevant coastal features and irregular boundaries.
233 In summary, the new interpolation methodology does not rely on standard local
234 interpolation techniques or local statistical analysis, but rather obtains a global trigonometric

interpolant, within a Fourier Analysis framework, through gradual interpolation of the target region (a multistage approach), making it more robust to overfitting. The theoretical basis for this methodology was recently developed by The Numericus Group, LLC, employing state-of-the-art mathematical algorithms. The use of the code should be coordinated by contacting The Numericus Group at info@thenumericusgroup.com.

3. Satellite SST Data Sets

The capabilities of the technique are illustrated through application to retrievals of SST from several current, commonly employed satellite sensors that span the range of available spectral type and spatial resolution. The products include infrared (IR) retrievals from the polar-orbiting MODIS from the NASA Aqua satellite and the geosynchronous Spinning Enhanced Visible and Infrared Imager (SEVIRI) on the Meteosat Second Generation (MSG- 2) satellite, and microwave (MW) retrievals from the Advanced Microwave Scanning Radiometer - Earth Observing System (AMSR-E) flown aboard the Aqua satellite. The testing described in this paper uses data from 8 February 2009 over the South Atlantic Ocean between 4N – 40S and 34W – 8E. Scenes from this day, as shown in Figure 1, were chosen because of the unusually high thermal IR coverage (few clouds obscuring MODIS and SEVIRI) and the presence of interesting large-scale thermal features such as a strong diurnal warming filament, clearly visible from all three sensors. An initial demonstration of the capabilities and limitations of the new technique additionally employs a composite of several days of SEVIRI data surrounding 8 February.

The MODIS retrievals (Figure 1a) are at 1-km resolution as obtained from the level 2 (original satellite scan line/spot geometry) product processed by the NASA Ocean Biology

Processing Group (OBPG) and downloaded from the NASA Ocean Biology Distributed Active Archive Center (OB.DAAC, https://oceancolor.gsfc.nasa.gov/). The study area was bisected by two ascending MODIS ground swaths, each composed of four 5-minute granules, over the period from 13:45 UTC in the bottom-right corner to 15:40 UTC in the upper-left corner. Initially, data with quality indices, QI, 0–1, i.e., cloud-free according to the OBPG quality indexing conventions for their MODIS SST product (0: Good, 1: Questionable/suspect, 2: potentially cloud/sunglint contaminated, and 3: bad/cloud contaminated/failure), were considered as an effort to minimize the size of the gaps in MODIS coverage and test the ability of the interpolant to recognize pixels with residual cloud contamination and potential inconsistencies in the quality indexing of the retrievals. It is important to emphasize that there is no uniform approach for satellite-derived SST quality flagging at present. For IR SST sensors, however, the quality indexing is generally tied to proximity to cloud.

The 5-km (0.05°) resolution SEVIRI SST product (Figure 1b) is produced at the Meteo-France/Centre de Météorologie Spatiale (CMS, Lannion, France) within the framework of the European Organisation for the Exploitation of Meteorological Satellites (EUMETSAT) Ocean and Sea Ice Satellite Application Facility (OSI-SAF) and was obtained directly from IFREMER (The French Research Institute for Exploitation of the Sea). The product is a gridded (level 3 collated), hourly product obtained by averaging data obtained at full resolution every 15 minutes (EUMETSAT, 2011). From its geosynchronous orbit centered over 0° longitude, SEVIRI provides continuous spatial sampling over a grid from 60S – 60N and 60W – 60E. The selected image in Figure 1 corresponds to 1500 UTC. Data corresponding to quality flags 2-5 were included. Additional quality indices beyond the "best" pixels (OSI-SAF QI convention: 0: no data, 1: bad, 2: very low quality, 3: low quality, 4: acceptable, 5: best) were again included to

281 increase coverage and to test the ability of the interpolating function to evaluate the data quality
282 assessment performed by the data producer.
283 The AMSR-E microwave SST data (Figure 1c) were obtained in level 2 format from
284 Remote Sensing Systems (RSS, http://www.remss.com/, Wentz and Meissner, 2004). The
285 retrievals have a native resolution of approximately 38 km, but there is a high degree of
286 oversampling. Initial analysis of the data considered quality indices 2–4 (RSS QI convention: 1:
287 bad, 2: suspect, 3: should-be-good, 4: good) to evaluate the need for additional screening as
288 described below. Note that AMSR-E retrievals are not affected by non-precipitating clouds and,
289 thus, the quality indexing is not based on proximity to cloud, but rather on proximity to
290 precipitation, ice, or land, and other factors affecting the quality of the MW retrieval such as sun
291 glint, high winds, and electromagnetic interference. Since the MODIS and AMSR-E sensors fly
292 on the same satellite, their spatial and temporal coverage is nearly coincident (see Figure 1a and
293 c).

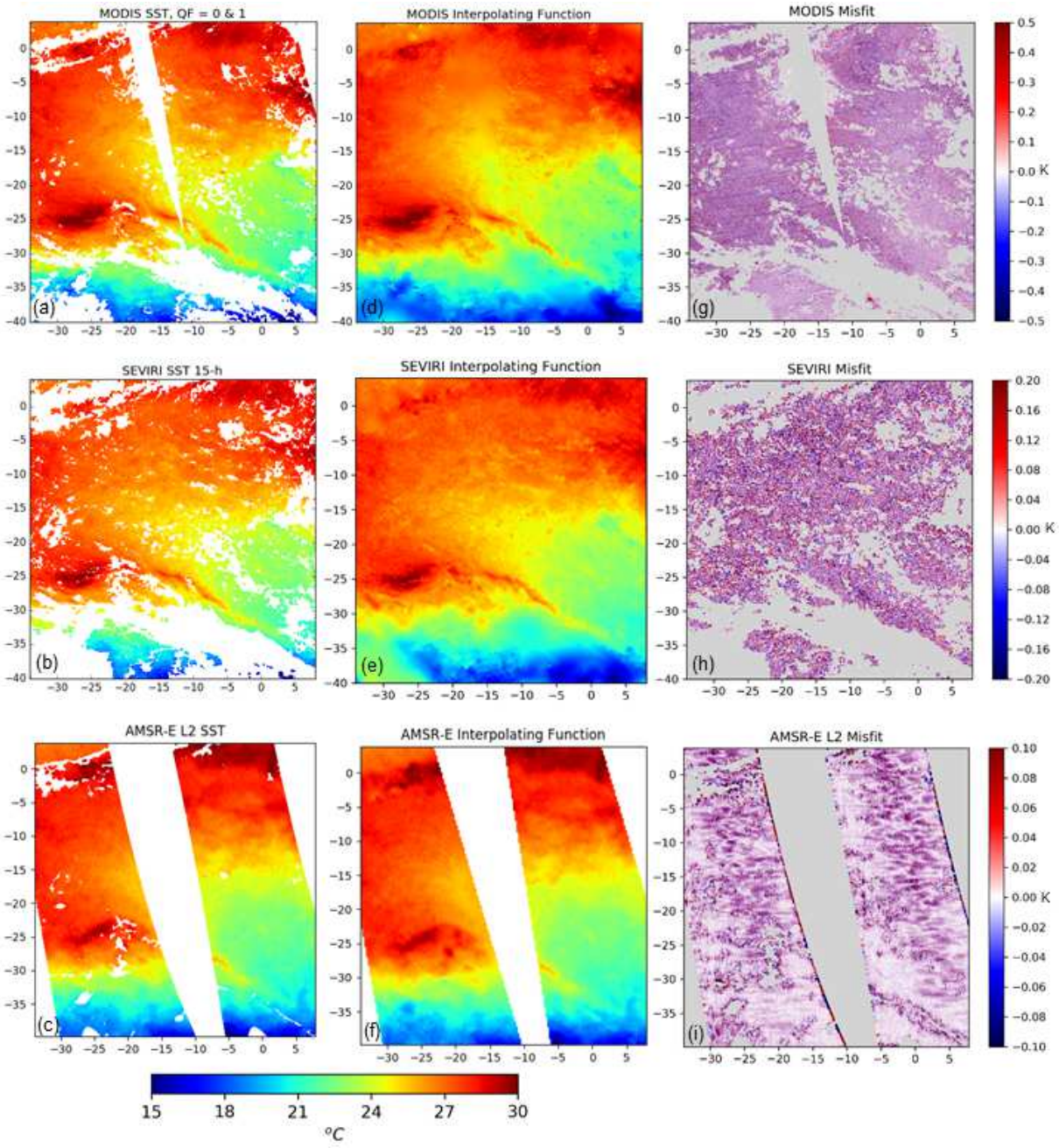

Figure 1. Illustration of (a-c) the input data to the interpolating function, (d-f) the resulting interpolant evaluated everywhere in the domain, and (g-f) the corresponding misfit for (top) MODIS, (middle) SEVIRI, and (bottom) AMSR-E. The input data shown has outliers already removed as described in Section 5. Panels a-f all share a common color bar shown at the bottom of the figure. Panels g-i have distinct color bars shown just to their right.

4. Demonstration of the Interpolation Methodology

An initial test demonstrates the new interpolation methodology's ability to both reproduce existing data and fill in data gaps. For this experiment, a spatially complete gridded data (no gaps) was required along with some realistic cloud mask. The basis for the data grid was a maximum value composite (MVC) generated from all hourly SEVIRI SST scenes over the study area over four consecutive days starting on 8 February 2009. To fill in a small number (less than 5%) of remaining gaps in the MVC, SEVIRI retrievals from the days prior to the starting day were inspected for additional observations at the empty grid cells. The first available observation, going backward in time, was used to fill the respective gap. The resulting SST scene is shown in Figure 2a.

To test the interpolation methodology, SST values corresponding to representative gaps due to cloud cover were removed prior to generating the interpolating functions. The source of this cloud mask was taken as the screened clouds from the 1500 UTC SEVIRI hourly product from 8 February 2009 as shown by the grey areas in Figure 2b. An interpolating function was generated using the remaining observations (clear pixels in Figure 2b), and then evaluated at every 0.05° grid point corresponding to the original, spatially complete, SEVIRI composite (all obs in Figure 2a). The resulting image is shown in Figure 2c. It is important to emphasize that at the locations where input data were available, the values shown in 2c are from the interpolating function and not the original retrievals. Qualitatively, the interpolating function is observed to do a good job in reproducing the original SST data in all but the regions with the largest assumed cloud cover.

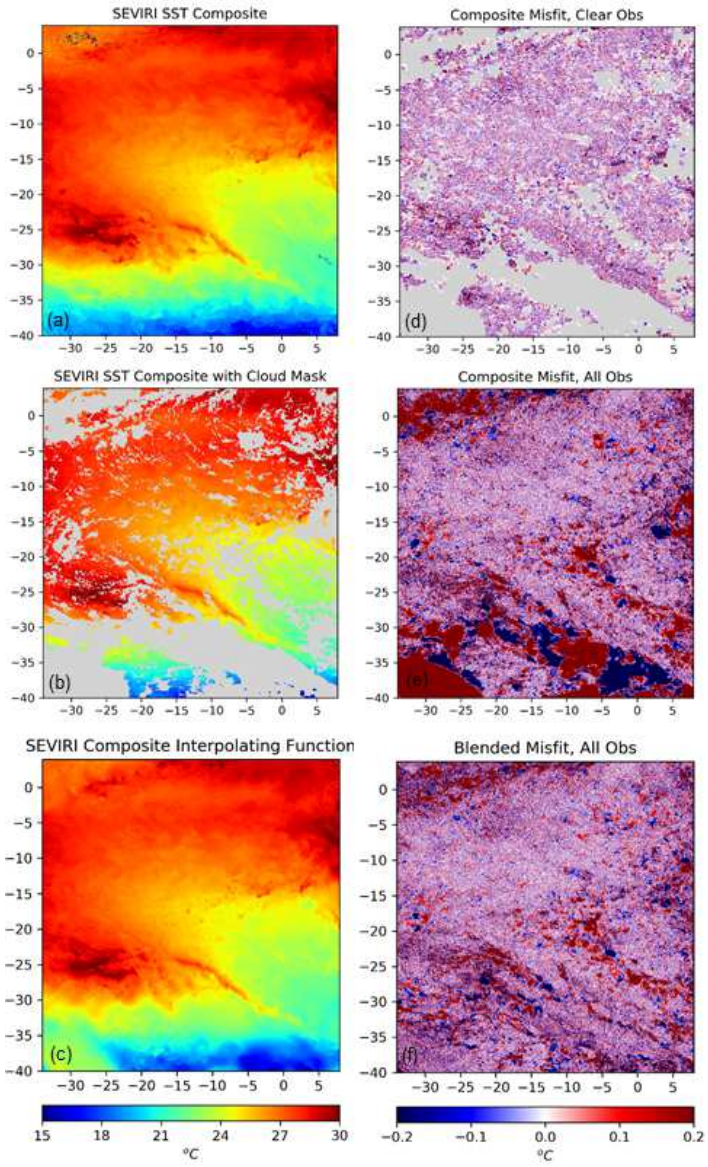

Figure 2. Initial demonstration of the interpolation technique applied to a SST composite derived from SEVIRI. Panel (a) shows the original composite, (b) shows the composite with the cloud mask applied, and (c) shows the interpolating function evaluated everywhere on the composite grid. The resulting misfit is shown in panels d-e for both the clear values and all values respectively. The corresponding "blended" misfit in panel e was derived in an additional experiment where additional inputs to the interpolation in cloud screened regions were supplied based on simulated lower resolution data. See text for details.

329

330 To quantify the accuracy of the interpolating function, the difference between the
331 functional value of the interpolant and the original SEVIRI SST composite was evaluated at each
332 grid point. Termed the "misfit," these differences are plotted for the clear observations from
333 which the function was derived (Figure 2d) and for all the points including the assumed cloud
334 gaps in the input data (Figure 2e). The misfit shows a speckle-like noise pattern with very small
335 amplitudes (within +/- 0.2 K) where the input data were available, demonstrating that the clear
336 observations are well reproduced by the interpolating function. As expected, however, the misfit
337 gets larger as the size of the gaps increases and, additionally, the speckle noise adds coherently
338 and self-organizes in large constructive and destructive patterns (the saturated red and blue
339 patches in Figure 2e corresponding to the largest gaps within the cloud mask). This shows that
340 the ability of the interpolating function to replicate the data within the gaps is constrained by the
341 size of the gap.

342 The misfit values from Figure 2e were then binned as a function of the Euclidean
343 distance to the nearest available observation to show how closely the interpolator replicates input
344 observations and to provide an indication as to how large of a gap can be effectively filled with
345 this technique. The results for gaps of increasing size up to 25 pixels (125 km) are shown as the
346 black trace in Figure 3. The misfit has a mean value of 0.10 K for the points at 0-distance (i.e.,
347 where observations were available) and then increases monotonically as the gap size (distance to
348 nearest observation) increases. If an acceptable accuracy for the interpolation error were
349 assumed to be 0.2 K, these results demonstrate that the technique is able to effectively fill gaps
350 of up to about 10 pixels (50 km) in size using the information contained in the available data.

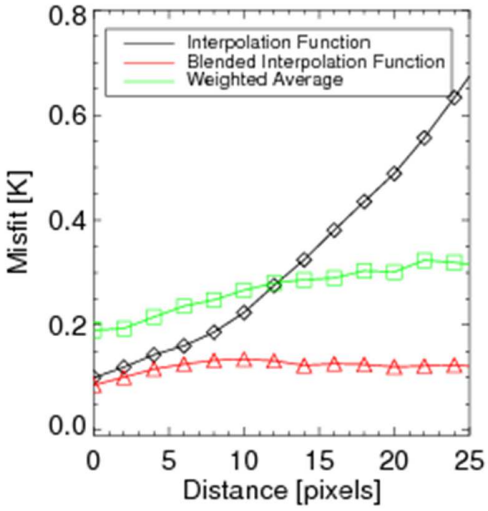

Figure 3. Mean misfit evaluated as a function of Euclidean distance to the nearest available observation for the identified interpolation techniques. The black trace reflects the results obtained from our interpolating function derived from inputs in clear areas only. The red trace was obtained from an alternative interpolating function obtained with additional simulated lower resolution SST input in the cloudy regions. The green trace applies to an independent simple distance-weighted interpolation approach. Solutions for this weighted technique exist only up to a distance of about 30 pixels.

While the focus of this paper is not on the skill of the interpolation at filling gaps, an additional experiment was performed to demonstrate how the method could be employed to fill larger coverage gaps as is done in existing SST analyses. In the regions where clouds were artificially introduced (Figure 2b), the original 5-km resolution SEVIRI composite data was replaced with a 25-km average value (i.e., 5x5-box averages of neighboring grid cells centered at each cloudy pixel) to simulate the availability of lower resolution AMSR SST retrievals under clouds. A new "blended" interpolating function (not shown) was generated based on this

367 combined data. The method was only allowed to utilize the additional lower resolution input
368 once the distance from the original higher resolution observations reached a user-specified
369 distance of 10 pixels. The misfit resulting from evaluating the blended interpolator at the initial
370 5-km SEVIRI composite SSTs is displayed in Figure 2f and the corresponding binning as a
371 function of the Euclidean distance to the nearest available observation is shown as the red trace
372 in Figure 3. The binned misfit reaches its maximum value at a distance-from-observation of
373 about 10 pixels corresponding to the transition to inclusion of additional data. Beyond this
374 threshold, the blended interpolator can be evaluated to fill larger and larger gaps with remarkable
375 accuracy and precision, as the misfit plateaus at 0.1 K for larger distances. For this idealized
376 case, where 25-km resolution data are assumed to always be available to guide the interpolation
377 when there is no high resolution data at hand and the coarser resolution data reasonably reflects
378 the SST patterns at finer resolution, the simple addition of the complementary coarser data
379 significantly improves the accuracy of the interpolator's spatial predictions at the unsampled
380 locations. It is for this very same reason that existing SST analyses blend data from multiple
381 satellite sensors.

382 Although we do not seek to directly compare the performance of different interpolation
383 methods, an additional test places these results in the context of an independent, alternative
384 method. A simple, distance-weighted, sphere-of-influence based interpolation technique was
385 also tested based on the available "cloud-free" observations in Figure 2b. For each grid point,
386 the technique searched for all available clear ocean observations within a radius of 100 km and
387 then computed the weighted average of those data with the weights given by one over the square
388 of the radius (inverse distance). Observations directly at the grid point (0 distance) were
389 assigned a weight of one. If there are no observations within the 100-km radius, the technique

390 fails to produce an estimate, and thus it cannot be used to produce complete fields. The misfit
391 between the weighted interpolation estimates and the original composite SEVIRI values was
392 computed and further binned with distance from the observations and shown by the green trace
393 in Figure 3. Within smaller gaps, our high-resolution multistage interpolation technique
394 outperforms the distance-weighted interpolation, but as the gap increases beyond about 12 pixels,
395 the localized weighted average does better than the interpolator derived from the cloud-free
396 observations. Although counterintuitive at first glance, a global interpolation method such as
397 ours uses global information content to fill in the small scale variability that in small gaps is
398 smoothed by the average, whereas in large gaps, the new method is conservative opting for
399 background values that are even smoother than a localized average. More detailed comparisons
400 of different techniques and application to filling gaps in multi-sensor data are deferred to a
401 separate paper.
402
403 **5. Application of the Interpolant to Scene Quality Assessment**
404 Beyond the basic illustration of the capabilities of the technique shown in the previous
405 section, the broader utility of the interpolation methodology can be demonstrated through
406 application to the individual sensor SST scenes described in Section 3. One such unique
407 application is helping to assess the quality of the data used to build the interpolating function,
408 including the identification of any potential artifacts in the input data.
409 Interpolating functions were generated for each of the sensor products in a two-step
410 approach: first using inputs with minimal quality control and a second step using refined inputs
411 obtained after removing outliers identified based on the magnitude of the interpolation errors
412 from the first step. In the preliminary screening, data from all the quality levels listed in Section

413 3 were used as inputs. This included data of more questionable quality that are typically
414 excluded in other applications, such as the construction of SST analyses (level 4 products). The
415 reason behind this approach is twofold: 1) to assess the ability of the interpolating function to
416 help with additional screening of poor quality data, and, 2) to retain as much data as possible to
417 build an interpolant able to accurately fill in gaps in coverage. So-called "questionable" data in
418 IR retrievals can be extremely challenging to screen using the conventional cloud masking
419 methodologies employed by most data producers. Traditional satellite cloud screening methods
420 rely on a series of thresholds to identify large retrieval errors. These techniques are not perfect,
421 however, as in many cases, such as with low stratus and polar maritime cloud, the clouds exhibit
422 very little contrast from the underlying sea surface. Thus, flagged observations often include a
423 mix of both contaminated and uncontaminated retrievals and valid data points may be discarded
424 when an entire quality level is excluded from an analysis.

425 The preliminary screening was successful in identifying contaminated observations
426 within the questionable levels while retaining other retrievals highly consistent with their
427 surrounding values. Interpolation errors were computed as the difference between the actual
428 satellite-retrieved SSTs used to derive the functions and the values of the interpolating function
429 at the locations (nodes) of the SST input. Note that unlike exact interpolators, the interpolation
430 error at the nodes is non-zero with the proposed method, accounting for uncertainty in the
431 observations. Distributions for the interpolation errors were obtained from normalized
432 histograms. Differences exceeding a specified threshold suggested unreasonable satellite
433 retrievals inconsistent with a smoothly varying SST field. Residual outliers identified in this
434 fashion were then rejected prior to generating the interpolating function. Sharp SST frontal
435 features or narrow patches of diurnal warming pose challenges where valid data could also be

436 rejected and represent a key tradeoff in selecting the rejection threshold. A high rejection
437 threshold, nominally based on the 99% quantile of the distribution of the differences, was
438 utilized in an effort to reject residual cloud contamination only.

439 The results reveal how the retrievals rejected in this manner compare to the quality
440 indices assigned by the data producers. The percentage of "best" and "suspect" quality
441 observations rejected is shown in Table 1 for MODIS and AMSR. No SEVIRI input
442 observations were rejected during the screening process. For MODIS, the observations were
443 screened using the SEVIRI-derived interpolating function rather than using direct comparison
444 against values of the MODIS interpolating function, as the SEVIRI interpolator was more
445 effective at identifying outliers given the higher levels of uncertainty in MODIS. For both
446 MODIS and AMSR, a larger percentage of the observations indexed as "suspect" by the data
447 producer were rejected, but some "best" quality observations were also removed.

448

449 Table 1. Percentage of original observations of specified quality index rejected in first stage
450 screening.

Sensor	Best Quality	Questionable Quality
MODIS	0.01% (QI 0)	1.05% (QI 1)
AMSR-E	1.0% (QI 4)	4.5% (QI 2)

451

452 In the second step, the input data retained after the exclusion of outliers in the screening
453 step were used to compute the final, refined interpolating function for each sensor. The quality-
454 controlled SST inputs are shown in Figure 1 a-c. The final degree, L_{final}, used for the
455 interpolating trigonometric polynomials was 1024 for MODIS, 512 for SEVIRI, and 256 for

AMSR-E. The degree was algorithmically derived as part of the multistage approach to build the interpolating function. The choice of the degree is the result of, at each stage, checking the size of the intermediate residuals and monitoring the condition number of the system to solve for the coefficients of the intermediate interpolating function. The polynomial degree reflects the ability of the interpolating functions to reproduce the observed variability without fitting residual noise in the data. The degree also reflects some correlation with the sensor product resolution. For efficiency in the current technique, degrees based on powers of 2 were used, but this will be generalized to any degree in the future. Because of the large gap between the AMSR-E swaths, separate interpolating functions were generated independently for the individual swaths. The manual separation of input data for the two swaths was performed for AMSR-E only.

To illustrate the performance of the code, we recorded the execution time needed to generate the interpolating function with the highest degree on a workstation with an Intel i7-7700K CPU operating at 4.2 GHz. The MODIS input (Figure 1a) contains 5,172,397 pixels and the interpolant constructed has degree 1024. Interpolant construction required 957 seconds (median of 3 timings, excluding I/O), that is, about 16 minutes. Next, we evaluated the interpolant on the whole domain displayed in Figure 1d (42 x 44 degrees) which contains 19,350,000 pixels. This evaluation required 37.4 seconds (median of 3 timings, excluding I/O). Our current implementation has not been heavily optimized, and we anticipate that significant acceleration is possible, especially in the construction of the interpolant. To expand the implementation of the technique to global applications would require partitioning the ocean basins into similar sub-domains.

The resulting values of the interpolating functions evaluated on full grids, corresponding to the resolution of the input data from each sensor, are shown in Figure 1 d-f. For AMSR-E,

479 due to the high degree of oversampling, a regular 0.25° resolution grid was used, consistent with
480 the corresponding level 3 products provided by Remote Sensing Systems. As before, at the
481 nodes where original data were available, the values shown are from the interpolating function
482 and not the original retrievals. Qualitatively, at the large image scale, the interpolating function
483 for each sensor captures the spatial SST variability extremely well, further illustrating the strong
484 potential of the technique. At nodes where input data were available, the interpolating function
485 accurately reproduces all major features, including the region of diurnal warming. Within the
486 original sampling gaps, the interpolated functional values generally appear physically realistic,
487 while providing a continuous SST field. Not surprisingly, as emphasized in the initial
488 demonstration in Section 4, the ability of the interpolating functions, derived based on single
489 sensor data as done in this demonstration, is more limited in regions of extensive data gaps such
490 as between satellite swaths. In these regions (e.g., Figure 1d), the functional values are notably
491 smoother, as the methodology takes a conservative approach in poorly sampled regions so as not
492 to introduce spurious fine resolution features. At the edge of the image domains where there is
493 no input data to bound the function, some larger errors can be observed, as the function is not
494 designed to extrapolate outside the spatial domain for which it was built.

495 The general skill of the interpolating functions in reproducing the underlying SST
496 structure and variability for the MODIS and SEVIRI satellite products can also be assessed
497 through comparisons with independent drifting buoy observations. Buoys have long been a
498 standard against which satellite SST retrievals have been judged. For this evaluation, quality
499 controlled drifting buoy data obtained through the NOAA iQUAM in-situ SST monitoring
500 system (https://www.star.nesdis.noaa.gov/sod/sst/iquam/; Xu and Ignatov, 2014) were compared
501 separately against the direct satellite retrievals and against values of the interpolating functions

for the scenes considered above both in regions where retrievals were available and in the gaps where no training data were available. For the direct satellite retrievals, buoy observations were matched with satellite retrievals within one hour in time and either the closest grid cell (SEVIRI) or the nearest retrieval (MODIS) within less than 20 km. With the interpolating function, the satellite SST is matched with the buoy by directly evaluating the function at the exact node corresponding to the buoy location. Since the MODIS image uses granules from 13:40 to 15:45 UTC, buoys present in the domain from 1300 to 1600 were extracted for the MODIS matchups. In the case of the 1500 UTC SEVIRI, buoys within 1400 and 1600 UTC were considered.

Statistics for the buoy comparisons are summarized in Table 2 and further support the skill of the derived interpolating functions. One notable result is that the rms difference with respect to the buoys within clear ocean pixels is smaller when using the interpolating function estimate than for the retrievals themselves for both MODIS and SEVIRI. The biases are also generally similar. These findings reflect positively on both the overall accuracy of the interpolating function and its ability to be evaluated at precise point locations. While the agreement between the buoy measurements and estimates derived from the interpolating function is somewhat degraded in cloudy regions for SEVIRI, the values are quite similar between the clear and cloudy regions for MODIS suggesting some value of the interpolated MODIS results within the cloud-covered gaps.

522 Table 2. Statistics comparing the SST values retrieved directly or obtained from the
523 interpolating function against collocated buoy SST measurements. The bias is computed as
524 retrieved value minus the buoy measurement.

Sensor	Satellite Retrievals			Interpolator in Clear			Interpolator in Clouds		
	Points	Bias (K)	STD (K)	Points	Bias (K)	STD (K)	Points	Bias (K)	STD (K)
MODIS	64	-0.16	0.60	64	-0.11	0.53	40	-0.14	0.60
SEVIRI	26	0.06	0.28	26	0.01	0.21	50	-0.07	0.66

525

526 A more quantitative pointwise evaluation of the resulting interpolation error at nodes
527 where the input data were available better illustrates the ability of the methodology to further
528 assess the quality of the underlying data. Residual differences (again termed the misfit) were
529 computed between the functional value of the interpolant at the location of the available satellite
530 SST retrievals and the actual retrieved SST values as in Section 4. Corresponding misfits for
531 MODIS, SEVIRI and AMSR are plotted in Figure 1 g-i, respectively. The typically small values
532 of the misfit again demonstrate how the function is able to accurately capture the observed SST
533 variability throughout the scene. Only for MODIS are residual differences comparable to, or
534 larger than, the expected satellite retrieval accuracies (about 0.5 K). Moreover, closer
535 examination of patterns in the misfit reveals how powerful the technique can be in identifying
536 potential remaining artifacts related to cloud contamination, instrumental effects, and sampling
537 errors.

538 Locations of the largest values of the misfit (i.e., the top 1 or 5%) are further highlighted
539 in Figure 4 as the points plotted in black. It is notable that the patterns suggested by the largest

misfit values are quite different for the different sensor types. This suggests that the differences cannot be simply ascribed to properties of the functional fit, but rather may be associated with the underlying data. Given that the exact cause of the misfit is not always known with certainty, the differences, however, must be carefully examined before concluding that they are indeed data artifacts. Statistics comparing these largest misfit values with all other points are shown in Table 3. The increase in the mean misfit for the largest differences is clear, particularly for MODIS.

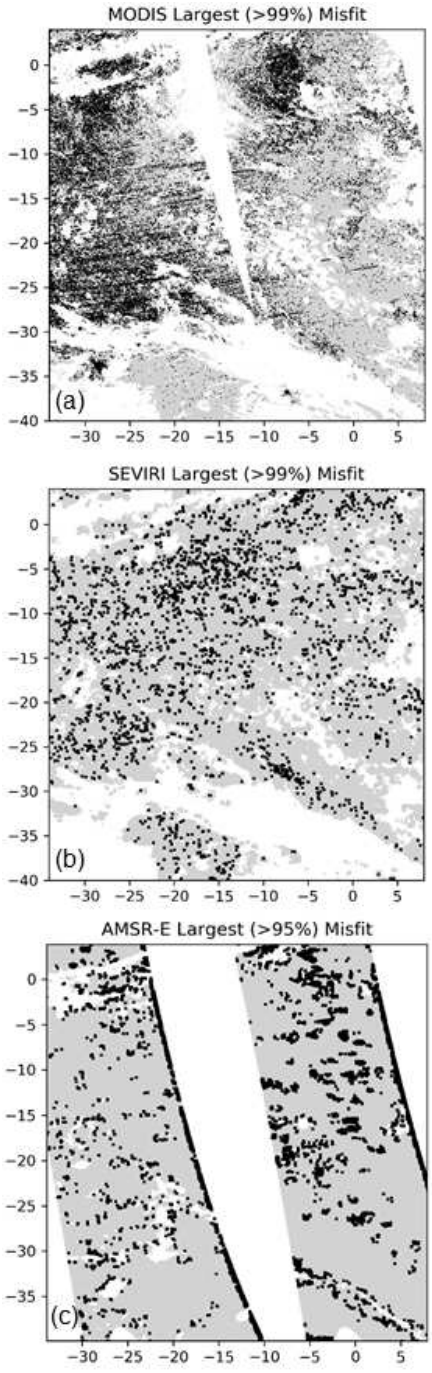

546

547 Figure 4. Locations of the largest misfit values for (a) MODIS, (b) SEVIRI, and (c) AMSR-E.

548 The locations exceeding the percentile indicated in the title of each panel are plotted in black

549 while all other observation locations are plotted in gray.

550

Table 3. Statistics characterizing the difference in misfit for those points above and below the percentiles selected for the greatest differences between the observed and estimated SSTs.

Sensor		< 99%			> 99%		
		Points	Mean (K)	STD (K)	Points	Mean (K)	STD (K)
MODIS		5,120,673	0.12	0.01	51,724	0.58	0.11
SEVIRI		282,333	0.06	0.05	2852	0.28	0.04
AMSR-E		< 95%			> 95%		
	L Swath	85,790	0.02	0.02	4515	0.19	0.13
	R Swath	95,639	0.02	0.01	5034	0.13	0.10

The MODIS misfit maps (Figure 4a and 1g) show stripes consistent with individual scan lines from the sensor, particularly in the western swath. Scan striping has long been a problem for MODIS SST retrievals resulting from the use of an array of independent detectors with imperfect relative calibrations and a multi-sided (cross-track) scan mirror (Gumley, 2002). Substantial effort has gone into reducing the impact of scan striping, and the results have improved to the point where striping cannot be visually detected in the input MODIS scene in Figure 1a. Comparison of the smooth functional form and the retrieved data, however, suggests that striping is still present in the retrievals. Identification of striping at this low magnitude is challenging, and few other existing techniques have exhibited the ability to show the striping as clearly as the interpolating function does here.

The other most coherent regions of misfit for MODIS (Figure 2a) are found in regions just left of the scan center in the northern portion of the scene. The cause for this misfit pattern is not fully understood, but the region in the eastern swath does show correlation with a discrete

567 portion of the scan geometry suggesting that the effect could again be instrumental in nature.
568 Other isolated larger differences could have contributions both from sampling effects and
569 limitations in the functional fit. Instrumentally, the differences could indicate random noise or
570 potential problems with residual cloud contamination or subpixel cloudiness in the
571 corresponding SST retrievals. With respect to the functional fit, very fine scale variability at the
572 MODIS resolution might not be fully resolved given the tradeoff between distinguishing natural
573 high frequencies from noise.

574 The magnitude of the misfit can again be compared to the original quality flags assigned
575 by the data producer. Using MODIS as an example, the mean misfit expressed as a function of
576 the quality index is presented in Table 4. Results are shown both for the absolute value of the
577 misfit and for the true mean where positive and negative values can partially cancel out. As
578 noted before, the mean misfit is very small in magnitude, reflecting the overall goodness of the
579 functional fit. A slight increase in magnitude of the misfit is observed for the "questionable"
580 data quality that was retained following the initial step removing outliers, but the fact that the
581 change is so small further justifies the inclusion of the additional data in the analysis.

582

583 Table 4. Mean magnitude of the misfit in the MODIS interpolating function expressed as a
584 function of quality index.

	Best Quality	Questionable Quality
Mean Misfit (K)	0.00	-0.01
Mean Absolute Misfit (K)	0.12	0.16

585

586 The SEVIRI misfit (Figure 4b and 1h) exhibits a largely random pattern with the
587 exception of a concentration of larger misfit values along the axes where diurnal warming is
588 observed to be greatest. For these areas near strong diurnal warming, the source of the difference
589 is likely algorithmic rather than physical as the interpolating function may be overly smoothing
590 across the sharp SST gradients. The diurnal warming introduces stronger gradients than
591 elsewhere within the scene and forcing the interpolating function to resolve these gradients
592 would have resulted in the introduction of high-frequency noise. This is another clear instance of
593 the balance between resolving high-resolution features (i.e., preserving the interpolator from
594 over-smoothing) while keeping high-frequency noise to a minimum. Elsewhere, the large
595 differences do not appear to suggest any correlation with potential residual cloud contamination
596 in the retrievals with more suspect quality levels, suggesting that the majority of the cloud
597 contaminated data have indeed been excluded by the data producer. This again suggests that use
598 of lower level quality data does not necessarily have a negative impact; in fact for this
599 application, the inclusion of additional data might have been highly beneficial since other results
600 (Castro et al., 2014) have suggested that extreme diurnal warming events tend to be flagged as
601 poor quality data by the automated quality control processes implemented with operational data.
602 The AMSR-E misfit values (Figure 1i) are very small overall (about 0.1 K), but do show
603 some tendency for larger values (Figure 2c) to concentrate along the edges of screened
604 precipitation regions (the main source of the gaps inside the swaths of the AMSR-E input), swath
605 edges, and near the swath center. The concentration of elevated misfit values forming “halos”
606 around the pre-screened features suggest that additional unflagged retrievals in the vicinity of the
607 features might still be modestly impacted by the contamination source. While the functional fit
608 could also potentially over-smooth across edges in data coverage, the fact that such similar halos

609 are not observed for the other sensors lends support for unflagged rainfall contaminated pixels.
610 The interpolating function is also able to highlight known anomalies in the retrieved values at the
611 outermost spots on the right side of the scan. The increased misfit corresponds to known
612 contamination caused by parts of the Aqua spacecraft entering the field of view of the first (right-
613 most) pixels of each scan. These pixels are excluded in creation of the Remote Sensing Systems
614 level 3 products but are included with the level 2 data (Wentz and Meissner 2004). The misfit
615 values just to the right of the scan center could possibly suggest very small calibration
616 differences with scan spot, but these are much smaller than the expected retrieval accuracy.
617 Interestingly, while there is some correlation between the larger errors and scan spot, there is no
618 suggestion of correlation with scan line. The larger pixels at the left edge of the scan are due to
619 numerical issues with the interpolator at the boundaries of the interpolated swath areas, as it is
620 not equipped to extrapolate outside areas for which it was built. Recall that in the AMSR-E case,
621 two separate interpolants were constructed due to the wide gap between swaths. Careful
622 examination of the AMSR-E image in Figure 1c reveals the presence of periodic conical scan
623 patterns in the SSTs along the satellite tracks, especially on the left swath, which is mimicked in
624 the interpolated data (see Figure 1f). Trigonometric polynomial interpolants are particularly well
625 suited for fitting periodic, smooth features. The fact that these patterns have smooth curvature
626 with an apparent periodicity spanning over long distances along the satellite ground track means
627 that it can probably be characterized by a sinusoid function, which explains the failure of the
628 trigonometric interpolator to identify it as an artifact in the AMSR-E data unlike with the linear
629 striping in MODIS.
630

6. Application to Sub-Pixel SST Variability

Another novel application of the interpolating function is to explore subpixel variability within satellite products of differing spatial resolution. In geophysical phenomena, the measurement of a physical variable associated with a point, x, in a two-dimensional space represents an average value over some continuum area. From a practical standpoint, however, we tend to associate a measurement with its point value, $Z = z(x)$. For instance, it is common to implicitly treat the satellite-retrieved SST for a pixel as a point value, particularly when validating it against in situ point observations, even though the measurement integrates the radiation coming from the entire area within the satellite footprint. There is an estimation error stemming from this representation because there always is spatial variability in nature. This is what in satellite remote sensing has been broadly termed the point-to-pixel discrepancy. The unresolved spatial variability has an effect on the perceived uncertainty of satellite-derived products when the satellite retrieval is validated using observations with significantly finer resolution than the satellite. Vinogradova and Ponte (2013) presented a good recent discussion of this impact on sea surface salinity observations from the Aquarius satellite.

Accurately quantifying the true variability is very challenging in practice and the results are inevitably tied to the size of the region/footprint and the resolution and density of the available observations. The concept behind an observationally-based estimation of spatial variability is to densely sample regions the size of the satellite's footprint using instrumentation of sufficiently high spatial resolution to capture all the scales of variability within the footprint. The variance of the high-resolution observations then provides a measure of the spatial variability within the coarser pixel. This challenge is currently met through advances in technology with small, high resolution instruments mounted on fast moving platforms, with the

654 capacity to obtain measurements that fully resolve the finer scales of variability. While viable,
655 these field campaigns are expensive and cannot be conducted globally. Another option,
656 employed by Vinogradova and Ponte (2013) in the study of salinity, is to utilize high-resolution
657 model output fields in the place of direct observations to represent the variability within a given
658 footprint.

659 To estimate the subpixel variability within coarser resolution products, it is also possible
660 to use measurements from higher resolution satellite observations. The limiting factors of this
661 approach are the spatial resolution of the available satellite sensors, and obtaining sampling with
662 adequate density to accurately estimate the true variability of the field. While the first problem is
663 constrained by the available data, use of the interpolating function can potentially help with the
664 latter. Estimates of variability obtained exclusively from satellite retrievals are limited by gaps
665 and the underlying noise of the data. Collocation and direct aggregation of all observations
666 within successively larger footprints is also computationally expensive. In contrast, interpolating
667 functions derived from the high-resolution observations are continuous (gap free) and can be up-
668 scaled or integrated easily over larger areas corresponding to the coarser resolution products.
669 Thus, interpolating functions have the advantages of providing physically consistent values
670 everywhere within the desired coarser footprints (aside from the largest gaps), ease of analysis,
671 and smoothing out other sensor-specific noise that could affect direct averages and variability
672 estimates.

673 Since the interpolant $I(x, y)$ described in (1) is an explicit trigonometric polynomial of
674 two real variables, we can efficiently compute its moments over any desired region by reducing
675 the problem to an application of the FFT or the USFFT. We are particularly interested in the
676 second central moment of the function to estimate the variance of the field. The aim is to

677 compare this estimated variance with the direct sample variance of the high-resolution pixels as
678 they are aggregated over successively coarser resolution grids. This estimated variance can, in
679 turn, inform estimation of the subpixel variability and its contribution to an uncertainty budget of
680 satellite SST retrievals.

681 The differing resolutions of MODIS (1 km), SEVIRI (5 km), and AMSR-E (25 km for
682 the level 3 grid) provide a means to investigate the subpixel SST variability on retrievals of
683 scales from approximately 5–25 km. The MODIS interpolating function can be used to estimate
684 variability within the SEVIRI and AMSR pixels and the SEVIRI interpolating function can be
685 used as an independent estimate of variability within the AMSR-E footprint.

686 Prior to using the interpolating functions to infer the spatial variability, it is useful to
687 further verify their ability to accurately estimate the mean SST field over the selected coarser
688 resolution footprints (e.g., the ability of the MODIS interpolating function to estimate an
689 observation over the coarser AMSR footprint). If the interpolating function accurately represents
690 the underlying physical field, the integral of the interpolant over the footprint should
691 approximate the satellite-retrieved value for that footprint. To test the functional approach, the
692 integral of the interpolants over coarser resolution footprints was compared against direct
693 arithmetic averages of all the available higher resolution observations within the same domain.
694 There is a caveat, however, in that the comparison involves the mean of a continuous function
695 over the integration domain and the average of a discrete sample with gaps in coverage. Missing
696 observations within the gaps are expected to contribute to differences with the interpolant
697 integral, but the comparisons can also provide insight into how consistently the gaps are filled in
698 by the interpolant. Note that the integral could also be compared with the original coarser
699 resolution observation on that footprint (say a 5-km integral of the MODIS interpolant with the

700 corresponding native 5-km SEVIRI retrieval), but that would introduce an intercomparison
701 between sensors with different characteristics that we want to avoid. Here, we wish to evaluate
702 the ability of the interpolants to supplant the direct, higher resolution observations from which
703 they were derived.

704 Results are shown in Figure 5 for comparison of the MODIS integrated interpolating
705 function and corresponding averaged MODIS observations on the SEVIRI and AMSR-E grids,
706 and the SEVIRI function and observations on the AMSR-E grid. The differences do not, in any
707 way, reflect measurement errors between different sensor types. To first order, the functional
708 integrals agree very well with the averages of the data from which they were derived. Mean
709 differences are near zero (< 0.04 K) and coherent differences are relatively small in magnitude.
710 Overall, the largest differences, not surprisingly, occur on the edge of large data gaps. Increased
711 differences do also occur in stronger gradient regions and near the diurnal warming feature (25S,
712 25W) where SST variability is greatest and accurate averages are dependent on all possible
713 measurements (which may not be available). Those differences, however, are still generally
714 within expected retrieval accuracy.

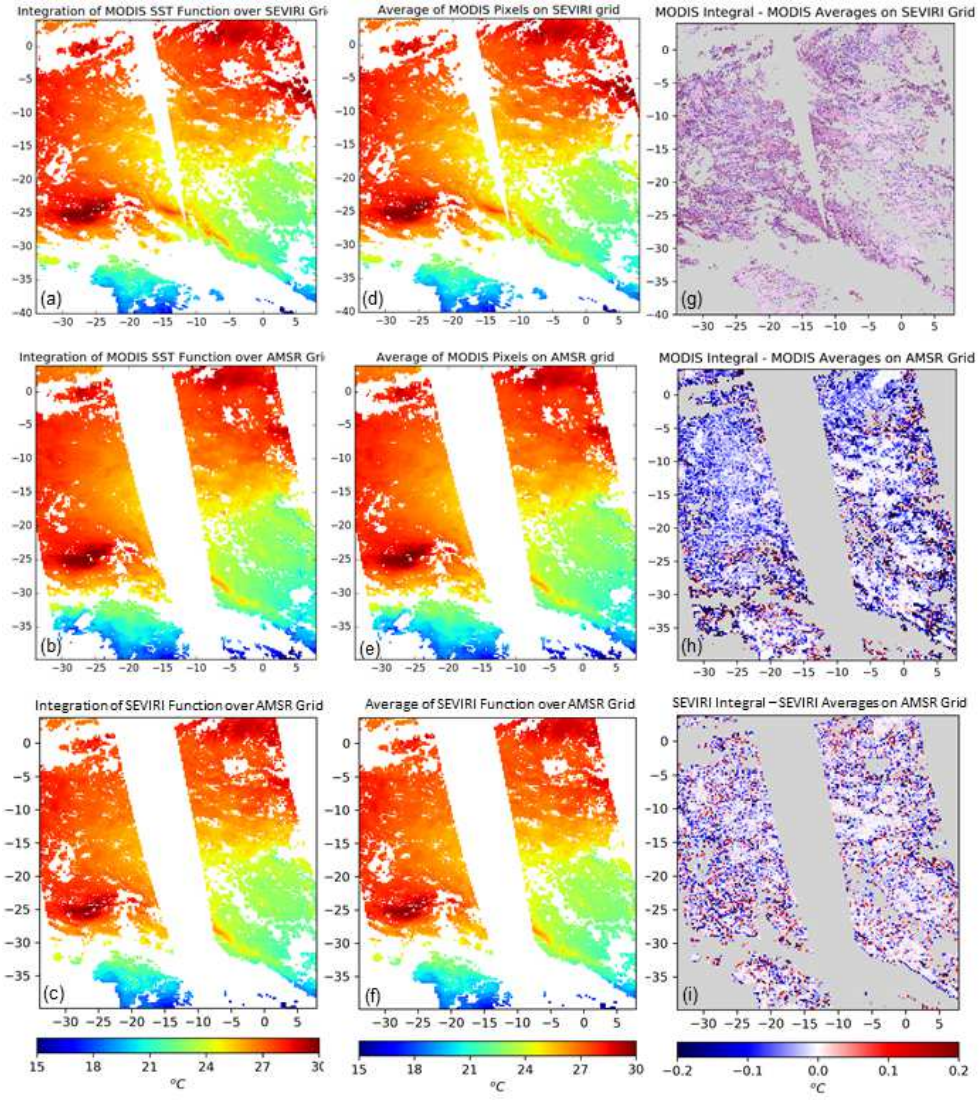

715

716 Figure 5. Evaluation of whether the integral of the interpolating functions is a direct analog to
717 the average of the underlying observations on the selected grids of differing resolution. The top
718 panels correspond to the evaluation of MODIS resolution sampling on the SEVIRI grid, the
719 middle panels to MODIS resolution sampling on the AMSR-E grid, and the bottom panels to
720 SEVIRI resolution sampling on the AMSR-E grid. Panels a-c show the integrals of the
721 interpolating functions over the grid cell, panels d-f show the average of the available
722 observations within the grid cell, and panels g-i show the corresponding differences between the
723 integrals and averages. Common color bars are shown at the bottom of each column.

724 To better appreciate the fine scale differences, the corresponding results for a smaller
725 region, centered on the large diurnal warming event, are shown in Figure 6. Distributions of the
726 difference values are also shown in Figure 7. Visually, the integrals of the interpolating
727 functions, again, appear very similar to the direct averages of the measurements and the
728 magnitude of the differences are reasonably small (mean differences all again < 0.04 K). For the
729 MODIS difference on the SEVIRI grid (Figure 6g), the effect of scan striping is again visible but
730 no other coherent patterns emerge. For MODIS on the AMSR grid (Figure 6h) the differences
731 are elevated near the large gradients associated with the region of diurnal warming and also near
732 the edges of coverage gaps. While the mean difference between the interpolant integral and
733 direct MODIS average on the AMSR grid is very small (-0.04 K), there is a skewness of the
734 difference distribution to negative values indicating that the value of the integral is typically
735 smaller than the average. This could potentially result from the presence of cloud "halos" or
736 slight residual cloud contamination on the edge of screened regions causing the interpolating
737 function to project slightly cooler SST values into the enclosed regions with missing
738 observations. The differences in the SEVIRI results evaluated on the AMSR grid (Figure 6i) are
739 quite random except for some enhancement on the edge of data gaps. The mean difference
740 between the integral and the sample average is less than 0.01 K. Overall, the results suggest that
741 the interpolating functions can accurately capture the variability within the coarser sensor
742 footprints and support further use of the functions to quantify this subpixel variability.

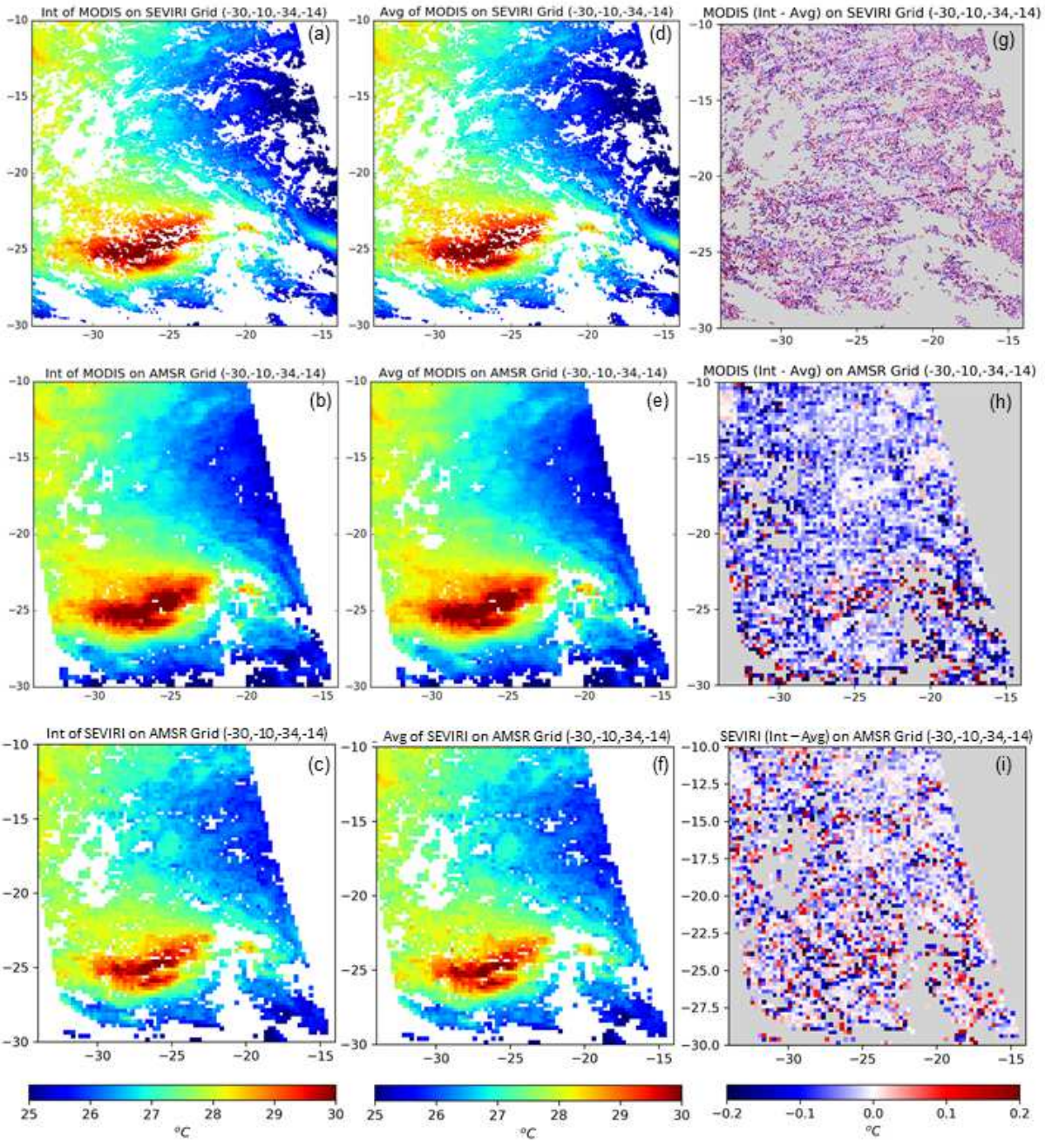

743

744 Figure 6. As in Figure 5, but for a localized region including the peak diurnal warming.

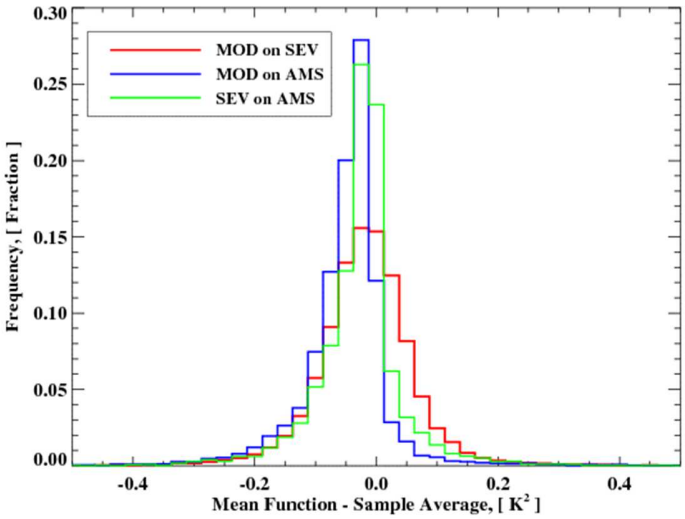

745

746 Figure 7. Distribution of the differences between the integrals of the interpolating functions and
747 averages of available observations for the results from the localized region plotted in Figure 6.
748 Results for the different sensor and grid combinations are plotted by color as shown in the
749 legend.

750

751 Based on this success, the ability of the second moment of the interpolating function to
752 characterize the variability within the coarser resolution pixels was explored next. The second
753 moment of the interpolating functions (or variance functions) was computed and integrated over
754 regions corresponding to the SEVIRI and AMSR-E footprints as for the first moment (the mean
755 of the function) above. These explicit variances were then compared with direct computations of
756 the sample variance for the corresponding higher resolution MODIS and SEVIRI measurements
757 within the same domains. Graphical results are shown in Figure 8 for the MODIS retrievals and
758 interpolating function evaluated on both the SEVIRI and AMSR-E grids, and corresponding
759 SEVIRI products on the AMSR-E grid. Distributions of the variance computed in both ways are

760 further plotted in Figure 9. A more detailed spatial comparison for the zoomed-in region with

761 enhanced diurnal warming is also shown in Figure 10.

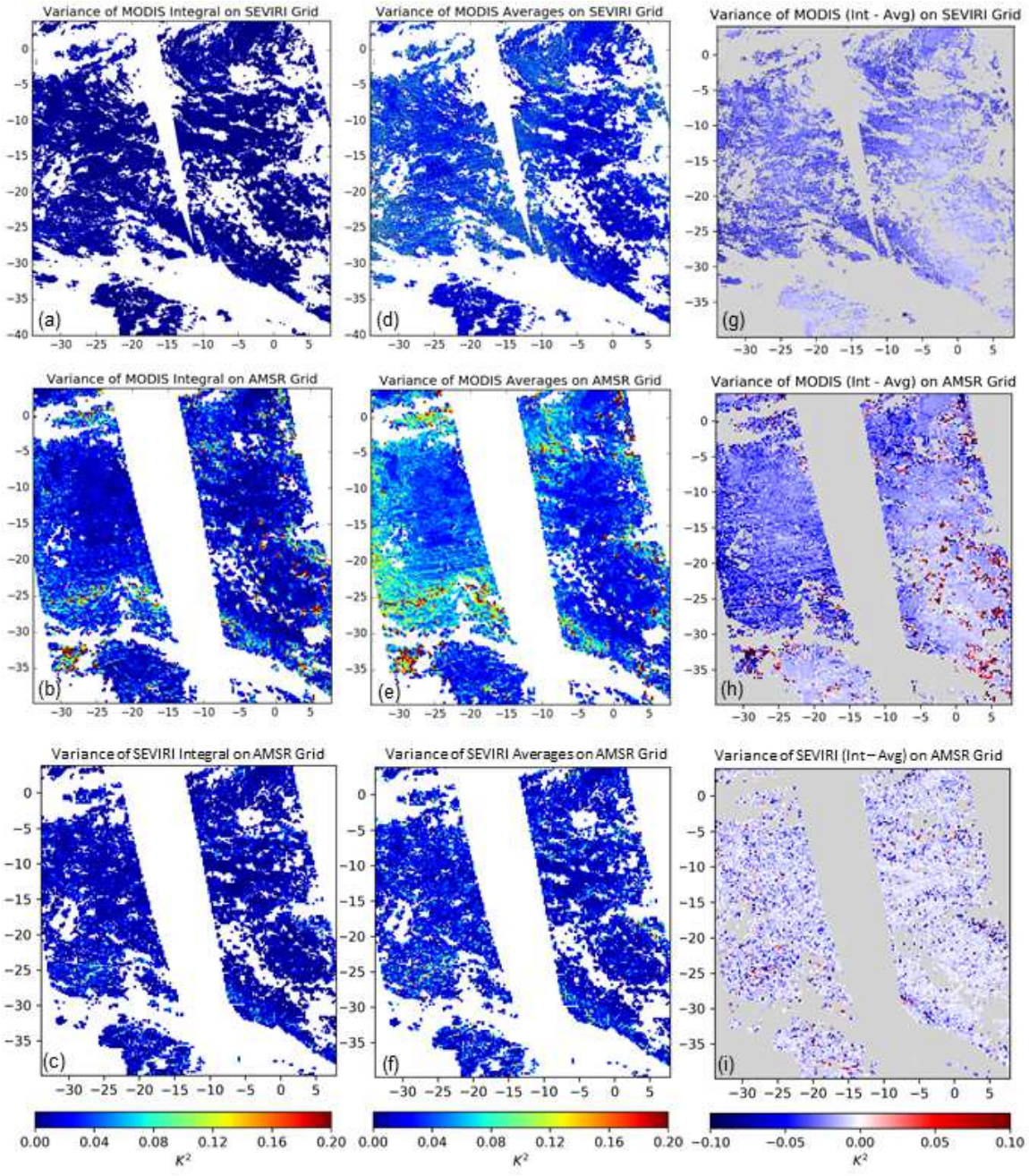

762

763 Figure 8. Evaluation of the ability of the second moments of the interpolating functions to

764 replicate the variance of the underlying observations on the selected grids of differing resolution.

765 The top panels correspond to the MODIS resolution sampling on the SEVIRI grid, the middle

766 panels to MODIS resolution sampling on the AMSR-E grid, and the bottom panels to SEVIRI
767 resolution sampling on the AMSR-E grid. Panels a-c show the variance computed from the
768 second moment of the interpolating functions over the grid cell, panels d-f show the variance of
769 the available observations within the grid cell, and panels g-i show the corresponding differences
770 between the functional and direct data approaches. Common color bars are shown at the bottom
771 of each column.

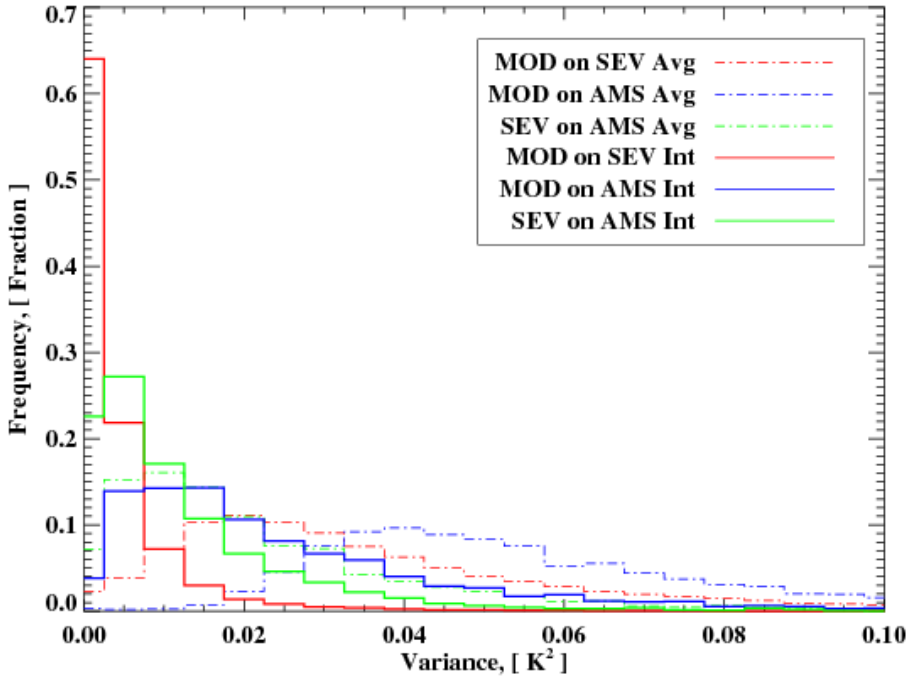

772

773 Figure 9. Distribution of the variance estimates computed from the (solid lines) second moments
774 of the interpolating functions and the (dotted lines) sample variance of the available observations
775 for the results from the entire domain plotted in Figure 8. Results for the different sensor and
776 grid combinations are plotted by color as shown in the legend.

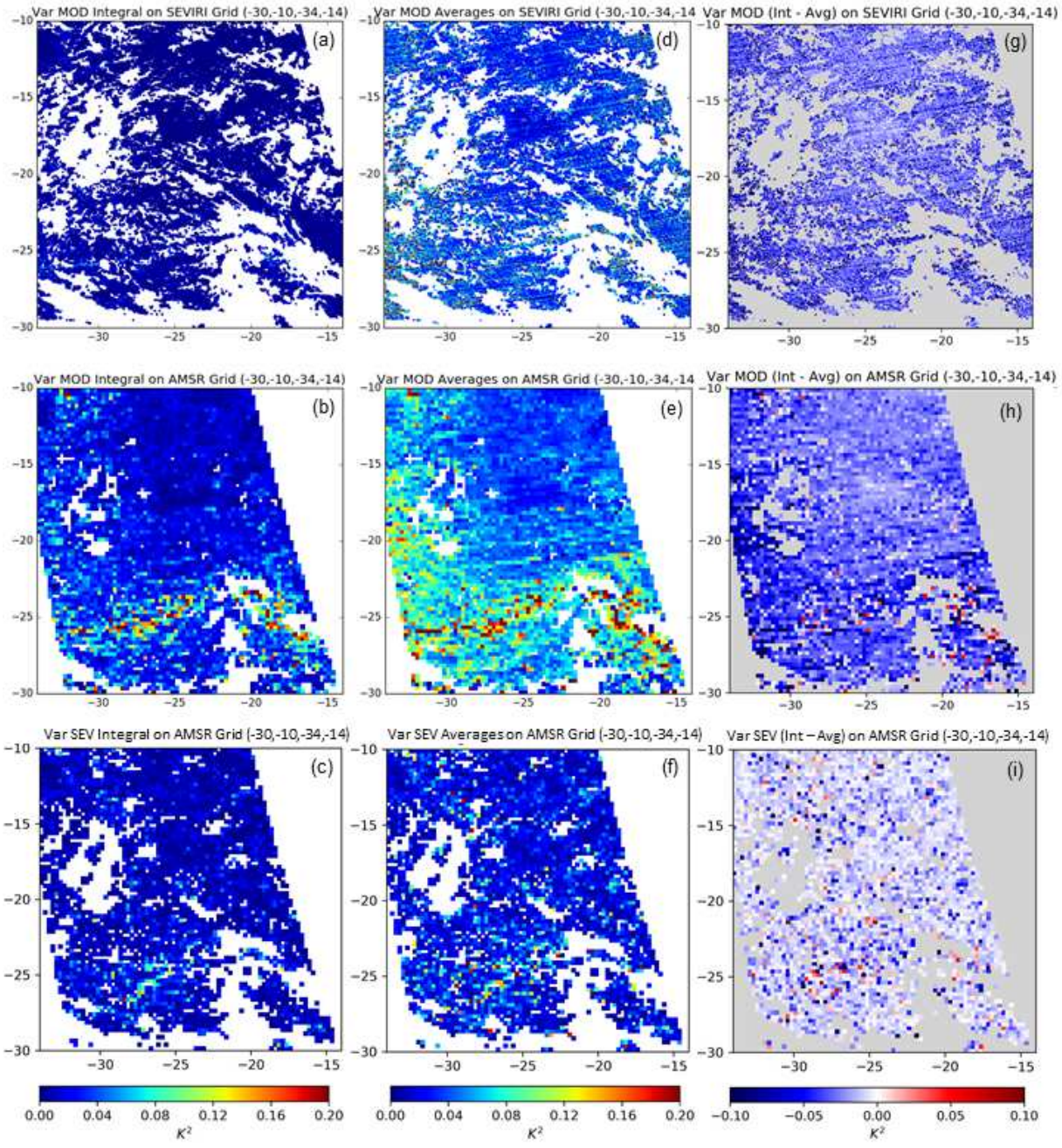

777

778 Figure 10. As in Figure 8, but for the localized region including the peak diurnal warming.

779

780 The dominant feature of the functional and observational variance differences is their

781 difference in magnitude. The variances derived from the interpolating functions are smaller in

782 magnitude than the sample variances of the observations over the same domains, but they reflect

783 similar regional patterns. No strong coherent spatial patterns are exhibited in the difference
784 images in either Figure 8 g-i or Figure 10 g-i.
785 Given the differences in magnitude between the variance estimates, it is important to
786 consider how representative the values are of the actual physical variability we wish to quantify.
787 An observational measure of spatial variability is dependent on the density of the underlying
788 sampling. Gaps in the observations can miss sources of variability. When observations are more
789 abundant, it is possible to get an increasingly better representation of the variability. Use of the
790 interpolating function allows estimation in the limit of complete sampling at the given resolution,
791 since they are continuous everywhere in the spatial domain for which they apply. This assumes,
792 of course, that the density of observations was at least sufficient to derive an accurate
793 interpolating function. Observational variability estimates are also critically dependent on the
794 noise level of the measurements. The presence of artifacts in the satellite retrievals noted in
795 Section 5 implies that the data might not be completely reliable for direct estimation of the
796 spatial variability. The interpolating function, in contrast, can largely mitigate the impact of
797 sensor noise and other artifacts. Because of the filtering of noise and some inherent smoothing
798 of the observations in the fitting process, the variability derived from the interpolating function is
799 expected to be lower in magnitude. Under conditions where the density of observations is
800 reduced (but not too low) and/or where the observations have elevated noise, the interpolating
801 function could provide an improved estimate of the true subpixel variability. At minimum, the
802 interpolating function should provide a lower physical bound on the spatial variability at the
803 scale of the underlying observations.
804 Based on this reasoning and the similar patterns in the derived variability, the variance
805 derived from integration of the second moment of the interpolating functions appears to provide

806 a powerful mechanism to help estimate the magnitude of, and regional differences in, the
807 variability within the selected satellite footprints. Comparison of the quantitative variance
808 estimates with grid resolution first provides insight into how the magnitude of the underlying
809 physical variability changes with spatial scale. Comparing variance estimates from the MODIS
810 interpolating function on the AMSR and SEVIRI grids shows increased variance over the larger
811 25-km AMSR cells (mean of 0.03 K^2 vs 0.005 K^2 for the full region). This is to be expected as
812 larger regions generally encompass increased spatial variability. The variance computed from
813 the SEVIRI interpolating function on the same AMSR grid (mean of 0.01 K^2) is less than that
814 from the MODIS interpolating function. This again makes sense as the higher resolution
815 MODIS observations resolve more small-scale variability than does SEVIRI, though perhaps
816 with increased noise. Lower limits on the derived variance, however, approach similar values in
817 open ocean regions. The mode of the variance of the MODIS interpolating function evaluated on
818 25-km regions is 0.005 K^2 (Figure 9) in agreement with the mean variance value evaluated over
819 5-km regions. This value corresponds to a standard deviation of 0.07 K, which is in excellent
820 agreement with the spatial variability contribution to satellite SST retrieval accuracy found by
821 Castro et al. (2010). The smallest variance estimates from the direct retrievals also approach
822 similar limits but show more variability across the satellite scans.
823 The variance estimates further permit closer examination of regional variations in the
824 spatial variability. For MODIS-scale 1-km observations aggregated on a 5-km resolution grid,
825 the explicit variance is very homogenous over the entire domain, with a barely noticeable
826 increase in the immediate vicinity of the peak diurnal warming (Figure 10a). The spatial
827 variability throughout is well captured by the mean variance value of 0.005 K^2. On scales of 25
828 km, however, localized areas with increased variance up to 0.2 K^2 are visible, particularly near

829 the diurnal warming. The peak values directly near the diurnal warming maximum obtained
830 from the direct retrievals are quite similar to those from the interpolating function, further
831 supporting this upper value. These results suggest that spatial representativeness errors on scales
832 of 5 km can be reasonably assumed to be around 0.07 K over large expanses of the ocean, but
833 that on scales of 25 km, localized variations should be considered and the errors can increase to
834 near 0.4 K in regions with enhanced spatial variability. Overall, these results obtained using the
835 new interpolating functions are broadly consistent with other localized estimates of spatial
836 variability, but further enable a practical way to help quantify spatial variability and
837 representativeness errors over much larger regions and at different scales.
838
839 **7. Conclusions and Future Directions**
840 A new powerful global interpolation technique yielding an interpolant in functional form
841 has been developed with multiple potential applications to the generation and analysis of
842 satellite-derived SST products. While directly relevant to the traditional application of gap
843 filling for construction of blended gap-filled analyses, the technique has additional novel
844 applications to the quality assessment of satellite SST retrievals and quantitative estimation of
845 spatial variability on different scales. Use in addressing these problems could provide important
846 guidance not readily available through other currently available methods.
847 The technique is based on the construction of a trigonometric interpolating function that
848 fits the input satellite retrievals within a limited spatial wavenumber domain, providing adequate
849 resolution in regions of larger data gaps and the highest possible resolution in regions with
850 sufficient data density. This resulting interpolant provides a functional representation of the
851 underlying physical SST field that can be evaluated anywhere within the domain over which it

852 was derived. Importantly, moments of the interpolating function can be calculated accurately
853 and efficiently, enabling estimation of the mean and variance of the field over desired sub-
854 regions. In this application, our choice of functional form was trigonometric polynomials to
855 assure speed of computation by using the FFT or the USFFT. Use of the technique was
856 demonstrated by application to level 2 satellite SST retrievals from the MODIS and AMSR-E
857 sensors and a level 3 gridded SEVIRI product as well as a spatially complete composite SST
858 product sampled with a realistic cloud mask.

859 The results illustrated how comparison of the functional form of the interpolant with the
860 original retrievals upon which it was based could be employed as part of an operational
861 processing scheme to help flag suspect retrievals for additional quality assessment. Large values
862 of misfit highlight specific retrievals potentially inconsistent with smooth variations of the
863 surrounding values. The technique was able to illustrate very small anomalies/artifacts such as
864 MODIS sensor striping largely undetectable with other approaches.

865 The choice of the functional form strongly affects what patterns can be identified. The
866 trigonometric polynomials employed in this application identified potential artifacts associated
867 with linear scan striping but fit and reproduced small conical stripes associated with the scanning
868 of AMSR-E. Alternate functional forms could be used to target other specific anomalies like
869 conical striping. In general, there are many known ways in which additional constraints can be
870 imposed to help filter out artifacts with specific characteristics and we plan to develop
871 appropriate interpolants for such purpose. The overall framework is extremely versatile and
872 powerful.

873 Direct comparisons between moments of the generated interpolating functions and the
874 observations used in their derivation showed that the technique can be used to accurately

875 represent spatial averages and quantify spatial variability in the underlying physical SST field.
876 Integrals of the interpolating functions for MODIS, SEVIRI, and AMSR-E agreed closely with
877 direct averages of the available retrievals over the same domains. This illustrates how the
878 interpolating functions can be used to emulate retrieval of the SST field at different effective
879 spatial resolutions. Moreover, the second moment of the interpolating functions was consistent
880 with the variability of the available observations within grids of coarser resolution demonstrating
881 that the functions can help provide quantitative estimates of, or bounds on, the spatial variability
882 on different desired spatial scales. The spatial variance estimated from the interpolating
883 functions was generally smaller than that of the direct observations due to observational noise
884 and the smoothing nature of the functions, but the values represent a lower bound on the physical
885 variability and could, in at least some cases, be more consistent with the actual variability on the
886 scale of the sampling given the observational limitations. Comparison of the interpolated results
887 with independent buoy SST measurements from the day assessed further supported the ability of
888 the technique to accurately reproduce the underlying SST field. Broader tests over larger regions
889 and additional days are, of course, desirable.

890 Quantitative estimation of the spatial variability of the SST on different scales and the
891 associated representation error of point and finer scale measurements is particularly challenging
892 with other traditional methods and much remains unknown about appropriate physical values.
893 Application of the technique provided new insight into the spatial SST variability, at least within
894 the limited region of this initial test. Within open ocean regions away from any frontal features,
895 variability of 1-km-resolution observations on grids of both 5- and 25-km resolution was found
896 to be ~0.07 K (as expressed by a standard deviation). In regions of sharper gradients such as
897 associated with strong localized diurnal warming, the variability within 25-km-resolution grids

898 increased to as much as 0.4 K for sampling at 1-km resolution. The variability of 1-km
899 observations on a 25-km-resolution grid was about 2.4 times greater than that on a 5-km-
900 resolution grid. Broader application of the technique globally could help better quantify true
901 regional variations in the spatial variability, which would subsequently improve uncertainty
902 estimates for existing satellite-based SST products.

903 The relative performance of the interpolation technique in the traditional gap-filling
904 problem as compared with other traditional methodologies was not explicitly examined in this
905 paper. Detailed comparisons are required to accomplish this in a meaningful way. Additional
906 activities related to this topic are planned and the utility of the technique for gap-filling in
907 construction of level 4 SST analyses will be explored.

908 While applied here primarily to single-sensor data, the technique can also be applied with
909 inputs from multiple sensors and observations collected across different measurement times to
910 handle larger data gaps as previewed in Section 4. Successful application of the interpolation
911 methodology is clearly dependent upon having sufficient observational data density and quality
912 to accurately derive and constrain the interpolating functions. As expected, the quality of the
913 interpolating functions is only as good as the data from which they are derived. The positive
914 outcome of this investigation was, in part, enabled by the low amount of cloud cover in the
915 scenes analyzed. Application of the technique, based solely on single-sensor data, will be
916 challenging in regions of extensive and persistent cloudiness where the infrared coverage can be
917 limited. Additionally, the finest effective spatial resolution of the interpolating functions is
918 naturally limited by the resolution of the data used in their derivation. Preliminary tests indicate
919 that the technique can be easily expanded to blend multi-sensor data to help ameliorate any
920 limitations associated with data density, which will further enhance the powerful new capability.

Acknowledgments

Participation of SLC and a portion of the time of LM was supported by a grant from the National Ocean Partnership Project for the Multi-sensor Improved Sea Surface Temperature (MISST) for the Integrated Ocean Observing System (IOOS) project (via NOAA award NA11NOS0120167). GAW was supported by NOAA in collaboration with the MISST for IOOS project. The satellite data sets utilized were all obtained from the providers as directly cited in the text. The efforts to ensure the open access to these data are greatly appreciated. The constructive comments of three anonymous reviewers are also acknowledged.

Declarations of Interest: none

References

Alvera-Azcárate, A., A. Barth, J.-M. Beckers, and R. H. Weisberg (2007). Multivariate reconstruction of missing data in sea surface temperature, chlorophyll, and wind satellite fields, *J. Geophys. Res.*, 112, C03008, doi:10.1029/2006JC003660.

Beylkin, G. (1995). On the fast Fourier transform of functions with singularities. *Appl. Comput. Harmon. Anal.*, 2, 363-381.

Bouali, M., and Ignatov, A. (2014). Adaptive reduction of striping for improved sea surface temperature imagery from Suomi National Polar-Orbiting Partnership (S-NPP) Visible Infrared Imaging Radiometer Suite (VIIRS). *Journal of Atmospheric and Oceanic Technology*, 31, 150–163.

943 Castro, S. L., Wick, G. A.; Minnett, P. J.; Jessup, A. T.; and Emery, W. J. (2010). The impact of
944 measurement uncertainty and spatial variability on the accuracy of skin and subsurface
945 regression-based sea surface temperature algorithms. *Remote Sens. Environ.*, 114, 2666-
946 2678, doi:10.1016/j.rse.2010.06.003.
947 Castro, S. L., Wick, G. A., and Buck, J. J. H. (2014). Comparison of diurnal warming estimates
948 from unpumped Argo data and SEVIRI satellite observations, *Remote Sens. Environ.*, 140,
949 789-799.
950 Castro, S. L., Wick, G. A., and Steele, M. (2016). Validation of satellite sea surface temperature
951 analyses in the Beaufort Sea using UpTempO buoys. *Remote Sens. Environ.*, 187, 458-475.
952 Castro, S. L., Emery, W. J., Wick, G. A., and Tandy Jr., W. (2017). Submesoscale sea surface
953 temperature variability from UAV and satellite measurements. *Remote Sensing*, 9, 1089;
954 doi:10.3390/rs9111089.
955 Chin T.M., Vazquez-Cuervo J., Armstrong E.M. (2017). A multi-scale high-resolution analysis
956 of global sea surface temperature, *Remote Sensing of Environment*, 200, 154-169, doi:
957 10.1016/.j.rse.2017.07.029.
958 Cornillon P., Castro, S., Gentemann, C., Jessup, A., et al. (2010). SST Error Budget – White
959 Paper. Available online: http://works.bepress.com/peter-cornillon/1/
960 Cressie, N.A.C. (1993). *Statistics for Spatial Data*. New York: John Wiley & Sons, Inc.
961 Dash, P., Ignatov, A., Martin, M., Donlon, C., Brasnett, B., Reynolds, R., et al. (2012). Group for
962 high resolution sea surface temperature (GHRSST) analysis fields inter-comparisons. Part 2:
963 Near-real time web-based level 4 SST quality monitor (L4-SQUAM). *Deep-Sea Res. II*, 77–
964 80:31–43, doi:10.1016/j.dsr2.2012.04.002.

965 Dutt, A., and Rokhlin V. (1993). Fast Fourier transforms for nonequispaced data, *SIAM J. Sci.*
966 *Comput*., 14, 1368-1393.
967 Esaias, W.E., Abbott, M.R., Barton, I., Brown, O.B., Campbell, J.W., Carder, K.L., Clark, D.K.,
968 Evans, R.H., Hoge, F.E., Gordon, H.R., Balch, W.M., Letelier, R., and Minnett., P.J. (1998).
969 An Overview of MODIS Capabilities for Ocean Science Observations. *IEEE Transactions on*
970 *Geoscience and Remote Sensing, 36*, 1250-1265.
971 EUMETSAT (2011). Geostationary Sea Surface Temperature product user manual.
972 SAF/OSI/CDOP/M-F/TEC/MA/181, Available online: http://www.osi-saf.org.
973 Gumley, L. (2002). *Proc. MODIS Workshop*. URL: Western Australian Satellite Technology and
974 Applications Consortium.
975 Hofstra, N., Haylock, M., New, M., Jones, P., and Frei C. (2008). Comparison of six methods
976 for the interpolation of daily European climate data. *J. Geophys. Res*., 113, D21110,
977 doi:10.1029/2008JD010100.
978 Kent, E.C., Challenor, P.G., and Taylor, P.K. (1999). A statistical determination of the random
979 observational errors present in voluntary observing ships meteorological reports. *Journal of*
980 *Atmospheric and Oceanic Technology*, 16, 905–914.
981 Martin, M., Dash, P., Ignatov, A., Banzon, V., Beggs, H., Brasnett, B., et al. (2012). Group for
982 high resolution sea surface temperature (GHRSST) analysis fields inter-comparisons. Part 1:
983 A GHRSST multi-product ensemble (GMPE). *Deep-Sea Res. II*, 77–80:21–30.
984 http://dx.doi.org/10.1016/j.dsr2.2012.04.013.
985 Minnett, P. J. (1991). Consequences of sea surface temperature variability on the validation and
986 applications of satellite measurements. *J. Geophys. Res*., 96, 18,475-18,489.

987 Murphy, R.E., Ardanuy, P., Deluccia, F.J., Clement, J.E., and Schueler, C.F. (2006). The Visible
988 Infrared Imaging Radiometer Suite. In J.J. Qu, W. Gao, M. Kafatos, R.E. Murphy, & V.V.
989 Salomonson (Eds.), Earth Science Satellite Remote Sensing: Vol. 1: Science and
990 Instruments. pp. 199-223. Berlin, Heidelberg: Springer Berlin Heidelberg.
991 Reynolds, R.W., and Chelton, D.B. (2010). Comparisons of daily sea surface temperature
992 analyses for 2007–08. *J. Climate*, 23, 3545–3563, doi:10.1175/2010JCLI3294.1.
993 Reynolds, R. W., and Smith T. M. (1994). Improved global sea surface temperature analyses
994 using optimum interpolation. *J. Clim.*, 7, 929-948.
995 Reynolds, R. W., Smith, T. M., Liu, C., Chelton, D. B., Casey, K. C., Schlax, M. G. (2007).
996 Daily high-resolution blended analyses for sea surface temperature. *J. Clim*., 23, 5473-5496.
997 Vinogradova, N. T., and Ponte, R. M. (2013). Small-scale variability in sea surface salinity and
998 implications for satellite-derived measurements. *Journal of Atmospheric and Oceanic*
999 *Technology*, *30*, 2689–914.
1000 Wentz, F. J., and T. Meissner, T. (2004). AMSR-E/Aqua L2B Global Swath Ocean Products
1001 derived from Wentz Algorithm. Version 2.
1002 Xu, F. and A. Ignatov, T. (2014). In situ SST Quality Monitor (iQuam). *Journal of Atmospheric*
1003 *and Oceanic Technology*, *31*, 164–180, doi:10.1175/JTECH-D-13-00121.1.
1004
1005

Figure Captions

Figure 1. Illustration of (a-c) the input data to the interpolating function, (d-f) the resulting interpolant evaluated everywhere in the domain, and (g-f) the corresponding misfit for (top) MODIS, (middle) SEVIRI, and (bottom) AMSR-E. The input data shown has outliers already removed as described in Section 5. Panels a-f all share a common color bar shown at the bottom of the figure. Panels g-i have distinct color bars shown just to their right.

Figure 2. Initial demonstration of the interpolation technique applied to a SST composite derived from SEVIRI. Panel (a) shows the original composite, (b) shows the composite with the cloud mask applied, and (c) shows the interpolating function evaluated everywhere on the composite grid. The resulting misfit is shown in panels d-e for both the clear values and all values respectively. The corresponding "blended" misfit in panel e was derived in an additional experiment where additional inputs to the interpolation in cloud screened regions were supplied based on simulated lower resolution data. See text for details.

Figure 3. Mean misfit evaluated as a function of Euclidean distance to the nearest available observation for the identified interpolation techniques. The black trace reflects the results obtained from our interpolating function derived from inputs in clear areas only. The red trace was obtained from an alternative interpolating function obtained with additional simulated lower resolution SST input in the cloudy regions. The green trace applies to an independent simple distance-weighted interpolation approach. Solutions for this weighted technique exist only up to a distance of about 30 pixels.

1029 Figure 4. Locations of the largest misfit values for (a) MODIS, (b) SEVIRI, and (c) AMSR-E.
1030 The locations exceeding the percentile indicated in the title of each panel are plotted in black
1031 while all other observation locations are plotted in gray.
1032
1033 Figure 5. Evaluation of whether the integral of the interpolating functions is a direct analog to
1034 the average of the underlying observations on the selected grids of differing resolution. The top
1035 panels correspond to the evaluation of MODIS resolution sampling on the SEVIRI grid, the
1036 middle panels to MODIS resolution sampling on the AMSR-E grid, and the bottom panels to
1037 SEVIRI resolution sampling on the AMSR-E grid. Panels a-c show the integrals of the
1038 interpolating functions over the grid cell, panels d-f show the average of the available
1039 observations within the grid cell, and panels g-i show the corresponding differences between the
1040 integrals and averages. Common color bars are shown at the bottom of each column.
1041
1042 Figure 6. As in Figure 5, but for a localized region including the peak diurnal warming.
1043
1044 Figure 7. Distribution of the differences between the integrals of the interpolating functions and
1045 averages of available observations for the results from the localized region plotted in Figure 6.
1046 Results for the different sensor and grid combinations are plotted by color as shown in the
1047 legend.
1048
1049 Figure 8. Evaluation of the ability of the second moments of the interpolating functions to
1050 replicate the variance of the underlying observations on the selected grids of differing resolution.
1051 The top panels correspond to the MODIS resolution sampling on the SEVIRI grid, the middle

1052 panels to MODIS resolution sampling on the AMSR-E grid, and the bottom panels to SEVIRI
1053 resolution sampling on the AMSR-E grid. Panels a-c show the variance computed from the
1054 second moment of the interpolating functions over the grid cell, panels d-f show the variance of
1055 the available observations within the grid cell, and panels g-i show the corresponding differences
1056 between the functional and direct data approaches. Common color bars are shown at the bottom
1057 of each column.
1058
1059 Figure 9. Distribution of the variance estimates computed from the (solid lines) second moments
1060 of the interpolating functions and the (dotted lines) sample variance of the available observations
1061 for the results from the entire domain plotted in Figure 8. Results for the different sensor and
1062 grid combinations are plotted by color as shown in the legend.
1063
1064 Figure 10. As in Figure 8, but for the localized region including the peak diurnal warming.
1065